Research article

Surface modification of AISI 316L stainless steel by applying single and multilayer coatings: Study of elastic modulus and antibacterial properties

Bahare Soltani, Sayed Mahmood Rabiee [*], Salman Nourouzi, Seyed Jamal Hosseinipour, Simindokht Khademjafari

Department of Materials Engineering, Babol Noshirvani University of Technology, Mazandaran, Iran

A R T I C L E   I N F O

A B S T R A C T

AISI 316L stainless steel is extensively used in various fields, including medicine. In this study, in order to improve antibacterial properties, reduce elastic modulus, increase hydrophilicity and delay corrosion on the surface of AISI 316L stainless steel pieces for biomedical applications, zinc and magnesium elements were used for coating. Zn monolayer, Zn-Mg bilayer, and Zn-Mg-Zn triple coatings were deposited on AISI 316L substrates using the thermal evaporation method. Field emission scanning electron microscopy (FE-SEM) confirmed the formation of thin film coatings on the substrate. EDX analysis also indicated the presence of Zn and Mg elements in the coatings. Atomic force microscopy (AFM) results showed a reduction in the root mean square roughness in the coated specimens compared to the uncoated ones. This technique was also used to compare the force between the samples. The result of this research indicated 22.78 % increase in hydrophilicity, 31.25 % improvement in antibacterial properties and 86.67 % reduction in elastic modulus when comparing the uncoated sample with the three-layer coated sample. X-ray diffraction (XRD) revealed the intermetallic composition of Zn and Mg. The average crystallite size, determined using Scherer's equation, was 14.61, 13.15, 13.92, and 49.60 nm for the uncoated, one-layer, two-layer, and three-layer samples, respectively. Atomic absorption spectroscopy (AAS) revealed that the 24-h release of Zn^{2+}, Mg^{2+}, and Ni^{2+} ions from the samples was within the allowable range when immersed in simulated body fluid (SBF). Corrosion measurements indicated the formation of a galvanic cell due to the layers in the coated samples, and the substrate did not corrode until the coating was fully degraded.

1. Introduction

AISI 316L stainless steel (SS) has been widely used in medical applications, particularly in implants (e.g., orthopaedics, dental prostheses, and bone screws) and surgical instruments (e.g., scissors, needle holders, tweezers, and pliers [1–3]. The biocompatibility and performance of SS implants have been confirmed over recent decades, as evidenced by numerous successful outcomes. Due to its appropriate fracture toughness, tensile strength, and fatigue resistance, this material has become the preferred choice for artificial joints in recent years [4]. However, despite its mechanical strength, SS has limitations such as a lack of antibacterial properties, poor

---

corrosion resistance, and a significant difference in elastic modulus compared to bone [3–5].

The considerable difference in elastic modulus between the implant and bone causes stress to be transferred entirely to the implant, while the surrounding bone experiences minimal stress. This situation can lead to bone atrophy and resorption. If the elastic modulus of the implant could be matched more closely to that of the adjacent bone, stress would be distributed to the bone as well, promoting bone regeneration [6–8].

Surface coating is one of the common methods to improve the properties of stainless steel such as its bioactivity and corrosion resistance and also enhance the fixation and functionalize the implant [9,10]. The elasticity modulus of the coating material is an important factor in its mechanical properties. Measurement of the elasticity modulus of such a limited-area and thin coating is impossible through conventional methods [6].

The atomic force spectroscopy is one of the most interesting research areas to study the surface interactions between a tip and sample in terms of force-distance curves. These curves can be employed to evaluate numerous properties such as elastic modulus, surface charge densities, and degree of hydrophobicity as well as the characterization of all types of surface forces [11,12].

Sub-micron monolayer and multilayer coatings have been recently employed for various applications. The layer-by-layer technique is a powerful strategy for surface modification with several potential applications in optoelectronics, nanofiltration, catalysis, and anti-corrosion and biomedical coatings [13–15].

The use of antibacterial coating can remarkably reduce the rate of post-surgery infection. Pathogenic species can damage healthy tissues and spread through the blood stream to the whole body, especially in extensive surgeries where a large incision is made and the surgical site remains open for a while. The junction between the implant and the tissue is a fibrotic inflammatory site where bacteria can easily attach and cause infection [16].

In recent years, doping has been an attractive method to gain some advanced properties of films. Tuba Yetim [17] proposed that the Ag-doped TiO_2 coatings could achieve higher corrosion polarization resistance in the SBF environment.

Thanks to their proper biocompatibility, non-toxicity, low density, and elastic modulus close to that of the human bone, Mg and its alloys have been extensively employed in medical applications such as cardiovascular and musculoskeletal fields. Mg is also a critical element in the human bone matrix. Mg^{2+} can stimulate the growth of bone tissue, whereby the bone marrow is regenerated by proliferating stromal cells [18–20]. Zinc is one of the most essential elements in the human body which supports many vital biological reactions such as protein and DNA synthesis. Zn is an essential factor in the production of alkaline phosphatase enzymes in bones and cartilage. Zinc alloys are applying increasingly in the field of biodegradable implant materials due to their unique combination of favourable biodegradability and good biological functions. Zinc element has antibacterial Properties and can also stimulate osteogenesis [12]. Zn ions promote bone growth by enhancing osteoblast differentiation and inhibiting osteoclast differentiation. Zinc implants, however, exhibit poor mechanical properties due to low ductility and relatively high density [21]. Thus, Zn coatings are often deposited on metals with high strength. Zinc is a well-known protective coating for steel. The incorporation of elements like magnesium into pure zinc coatings forms "Simonkolleite" which acts as a barrier against corrosive environments, reducing the corrosion current density and increasing corrosion resistance [4,22].

Due to the useful properties of zinc and magnesium elements that has been shown in the experiments, the use of combination of these elements as a coating was considered. Recently, some researches have been Conducted on coating the surfaces (of different materials) with Zn-Mg. In these researches the mechanical, chemical and anti-corrosion properties have been investigated [7]. In some researches, at first the surface has been coated with a pure Zn layer and then a Zn-Mg coating has been placed on it. The results have indicated thet this method leads to better adhesion of coating to the surface [16,20].

This study addressed the effect of single-layer Zn, double-layer Zn-Mg, and three-layer Zn-Mg-Zn coatings on the AISI 316L substrate to improve mechanical and antibacterial properties.

2. Experimental procedures

2.1. Preparation of samples

The AISI 316L stainless steel sheet, with a thickness of 2 mm, was cut into 20 mm × 30 mm pieces. The sample surfaces were polished using silicon carbide (SiC) abrasive papers, progressing through grit sizes ranging from 100 to 600. Afterward, to cover AISI 316L SS tablets with Zn, and Mg particles, substrates (AISI 316L SS tablets) were first ultrasonically decontaminated in distilled water for 25 min at 20 °C and dried at room temperature.

2.2. Thermal evaporation deposition

The coating process was performed by a thermal evaporation device (DTT). In this method, high-purity coating materials (99.99 %) including zinc and magnesium were placed inside the crucible. A power supply with a voltage of 8V and a current of 15A was employed to heat the crucible. The cathode-substrate distance was set to 20 cm. To prevent oxidation during the coating process, the pressure inside the sediment chamber was reduced to 5×10^{-5} torr, and the deposition was continued for approximately 1 min. This study compares uncoated samples with those coated by Zn monolayer (Z), Zn-Mg bilayer (ZM), and Zn-Mg-Zn triple-layer (ZMZ) coatings.

2.3. Surface characterizations

The phase and crystallographic structure of surface coating were explored by an X-ray diffractometer (XRD, Panalytical Empyrean,

Netherlands) with Cu Ka ($\lambda = 1.54$ A°) radiation over a 2θ range from 5 to 90°. The operating voltage and current were 40 kV and 40 mA, respectively. Crystalline species were identified using X'Pert High-Score Plus software.

Surface morphology and topography of the coatings were analyzed by field emission scanning electron microscopy (FE-SEM, MIRA3TESCAN-XMU, US & Auriga, Germany), coupled with an energy-dispersive X-ray (EDX or EDS) detector for elemental analysis. The extended surface topography was also measured by an atomic force microscope (AFM, Nano Wizard II, Germany) in non-contact mode. The roughness and elastic modulus of surface coating were assessed using AFM and Nanosurf Easy Scan 2 software. The AFM allows to scan the surface of objects at very high resolution and to translate it into numerical and visual surface data. Here, the mean roughness (Ra; arithmetic mean of absolute values) was utilized. In addition to the topography images, AFM can offer force measurements in nanometer range. These forces are the result of interaction between the surface of the sample and the tip of the cantilever. The elastic modulus of coatings was also evaluated by AFM. The AFM assessments were performed using triangular Si_3N cantilevers (145 μm long, with a spring constant of 0.18 nN/nm).
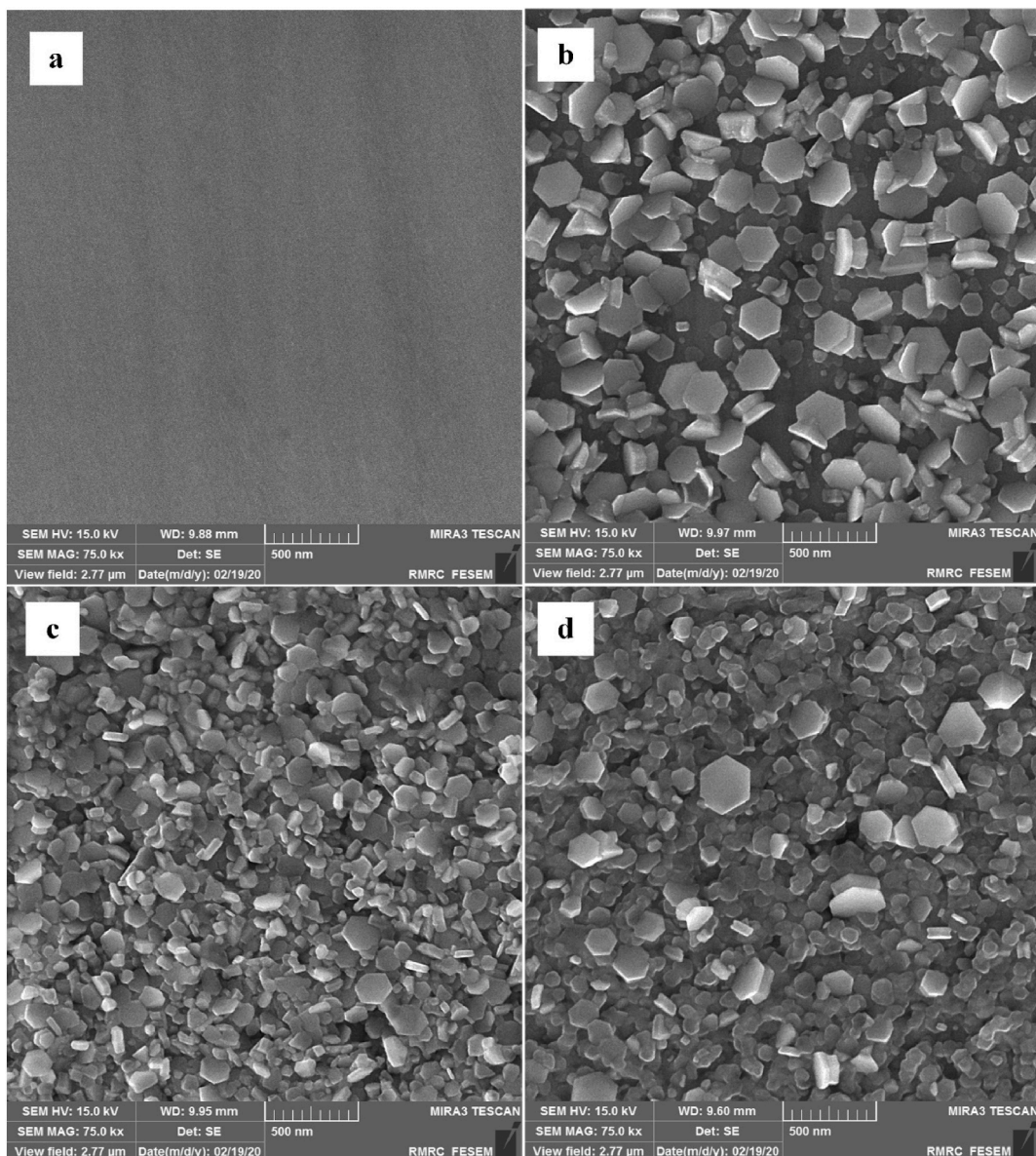

Fig. 1. SEM micrographs of surface Morphology of samples; (a) Un coated, (b) Zn coated, (c) Mg-Zn coated, (d) Zn-Mg-Zn coated.

2.4. In vitro experimental procedure

2.4.1. Wettability

The surface wettability was also examined by measuring the contact angle. A sessile drop of distilled water was deposited onto the surface using a video-based optical contact angle measurement system (OCA 15 EC, Data Physics Instruments GmbH, Germany). Lastly, the average contact angle of the left and right was taken to determine the contact angle.

2.4.2. Antibacterial activity

Antibacterial tests were carried out considering *Escherichia coli* as a gram-negative bacterium. First, the bacterial suspension was cultured in a test tube and incubated at 37 °C for 24 h to obtain the active generation of bacteria. Bacteria were then cultured on the inner surface of the plate cap and the coated side of samples was exposed to the bacteria. Then, the cap was placed on the plate. After 24 h, an inhibition zone was formed on the plate lid, indicating the extent of antibacterial power of the coating elements.

2.4.3. Release ions

The release of Zn^{2+}, Mg^{2+}, and Ni^{2+} ions from coated and uncoated samples was measured by an atomic absorption spectrophotometer. A simulated body fluid (SBF) solution was first purchased, and each sample was placed separately in an already prepared container. Each sample was tested in triplicates. SBF (20 ml) was poured into each of the containers. Subsequently, the sample and SBF solution were put in an incubator for 24 h at 37 °C. Afterward, the containers were removed from the incubator, and the SBF was withdrawn and measured by an atomic absorption spectrophotometer to determine the amount of released metal. Lastly, the average emission of all three similar samples was taken to obtain the results of this experiment.

2.4.4. Electrochemical properties

The corrosion resistance of the coatings was evaluated by Potentiodynamic polarization test and electrochemical impedance spectroscopy (EIS). Prior to these experiments, the uncoated parts of the samples were coated with epoxy. Electrochemical experiments were then performed by GAMRY Reference +600 electrochemical in SBF solution with pH of 7 at 36 ± 0.5 °C. The test surface of these samples was measured to be 1 cm^2. A typical three-electrode system was used for electrochemical experiments in which the platinum electrode, sample and a saturated calomel electrode served (SCE) as the auxiliary, working, and reference electrodes, respectively.

Before the test, all samples were immersed in SBF solution for 30 min to obtain a stable potential. After measuring open circuit potential (OCP), Potentiodynamic polarization diagrams were recorded by applying a potential voltage of −200 mV to + 500 mV against OCP at a scan rate of 1 mV/s. Flow density (*I_cor*) and corrosion potential (*E_corr*) were also analyzed according to TOEFL extrapolation. Data were analyzed using Z view software.
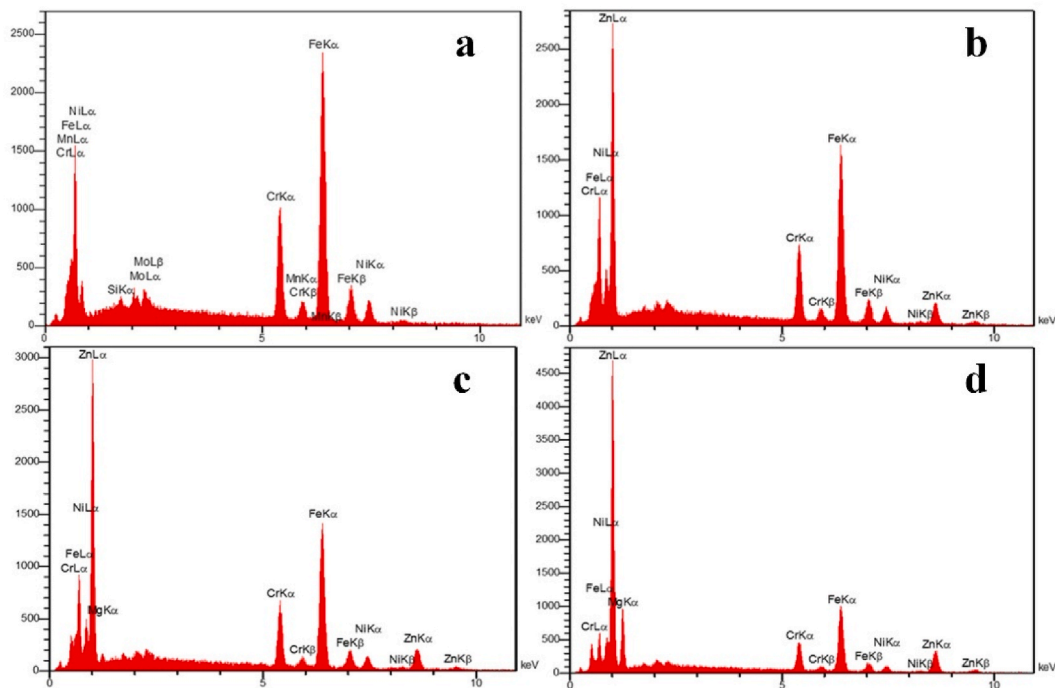

Fig. 2. EDX elemental analysis of samples; (a) Un coated, (b) Zn coated, (c) Mg-Zn coated, (d) Zn-Mg-Zn coated.

3. Results and discussion

3.1. Surface morphology and microstructure

Fig. 1(a–d) shows the field emission electron microscope images of the samples. As can be seen, the grain size of the samples was about 200 nm. The FE-SEM analysis revealed a similar surface structure across the multilayer coatings. The presence of small particles and cavities on the coatings' surfaces is likely due to the nature of the physical vapor deposition process. However, the surface of the triple-layer coating exhibited a more uniform appearance with fewer macro-particles and cavities, which can be attributed to its increased thickness. The EDX results presented in Fig. 2(a–d) showed that the weight percentage of Zn element in the uncoated, one-layer, two-layer and three-layer samples was 0, 21.89, 25.33 and 38.33 respectively, and the weight percentage of Mg element in the two-layer and three-layer samples was 0.95 and 11.19 respectively. SEM cross-sectional images of samples with Z, ZM, and ZMZ coatings are shown in Fig. 3(a–c). These results demonstrated that the coating thicknesses were within the expected range. Specifically, the thicknesses of the coatings in the Z, ZM, and ZMZ samples were 73.89 nm, 108.10 nm, and 145.97 nm, respectively.

Fig. 4 shows the XRD patterns of the uncoated samples and coated samples. Peaks corresponding to the austenitic stainless steel (Fcc γ-phase) can observed. In the case of the zinc-coated sample, the peak at 36° corresponds to the standard diffraction pattern of zinc element. The diffraction pattern of the sample with Zn coating was highly similar to the reference pattern of Zn element JCPDS card number: 65–3358. Intermetallic compounds of zinc and magnesium were observed in the two- and three-layer samples. XRD test results confirmed the presence of intermetallic compound Mg_2Zn_{11} [23]. The discharge time in thermal evaporation does not appear to be long enough for the Zn and Mg atoms to react. Thus, some pure Mg and Zn elements remained unreacted in the structure.

The average crystallite size can be estimated by Scherer equation (1):

$$D = \frac{K\lambda}{\beta \cos \theta} \tag{1}$$

Where β is the full width at half the maximum intensity (rad), λ represents the wavelength (λ = 0.154 nm), θ shows the Brags angle (°), K represents a constant (K = 0.9), and D denotes the crystallite size (nm). Half-width peaks (FWHM) were calculated using X'Pert High-Score Plus software.

The obtained results are listed in Table 1. The average grain size in all samples was under 15 nm except for the three-layer sample which was 49.60 nm. Average crystallite size of the uncoated sample, was 14.61 nm. This Parameter was 13.15, 13.92, and 49.60 nm in Z, ZM, and ZMZ coating samples, respectively.

AFM measurements were performed for topographic analysis of surfaces coated with Z, ZM, and ZMZ, as well as uncoated samples. Three-dimensional images were taken of the surfaces. The height distribution of the particle size in the Z direction of the thin coating surfaces of Z, ZM, and ZMZ samples can be found in Fig. 5(a–d). The roughness can be calculated along a profile as well as the surface (area). Profile Roughness (Ra) component and Surface Roughness (Sa) components are more commonly used to represent deeper and more important values. Sample surface roughness (Sa) measures the average size of surface peaks and valleys and also shows the standard deviation of the surface height distribution which (RMS = Sq), is the average square root of the samples. The values of Ra, Sa, and Sq of the uncoated and coated samples are listed in Table 2.

Accordingly, the surface roughness is almost equal in all samples. In other words, surface roughness has no role in the antibacterial properties of the samples. As the surface roughness increases, a mechanical connection is established between the implant surface and the cell, improving its adhesion to the implant surface and increasing the rate of osteoblast proliferation. The root mean square (RMS) of the uncoated sample, the one with one-layer, two-layer, and three-layer coating were 53.26 nm, 39.89 nm, 40.18 nm, and 42.99 nm and the average surface roughness (S_q) of the mentioned samples were calculated 41.32 nm, 30.23 nm, 32.90 nm, and 33.05 nm respectively. The average surface roughness of the uncoated sample was higher than the coated ones. Coating led to a more uniform surface roughness, providing better growth and proliferation of osteoblast cells and better bonding between the implant and the bone.

3.2. Elastic modulus of the surfaces

The AFM test was employed to compare the elastic moduli of the sample surfaces. It is well-known that the elastic modulus of metals, particularly stainless steel, is significantly different from that of bone. If an implant with a much higher elastic modulus is placed adjacent to bone, the implant will absorb most of the stress, potentially leading to bone atrophy. Therefore, it is crucial to reduce the elastic modulus of the samples to better match that of bone. The mechanical properties, including the elastic modulus and adhesion force of these samples, were evaluated using Atomic Force Microscopy (AFM). The experiments were conducted in air using the non-contact mode of the AFM. After acquiring topography images in non-contact mode, Force-Displacement curves were generated at various points on the sample surfaces using distance-dependent measurements available in the AFM software. In these tests, the AFM indenter tip, mounted at the end of a cantilever beam, was displaced towards the surface by a piezoelectric actuator. As the cantilever approached the surface along the Z-axis, its deflection was measured by a laser reflecting off the back of the cantilever onto a position-sensitive photodiode, producing an output voltage signal. This voltage signal was then converted to cantilever deflection by a sensitivity factor obtained from the slope of a linear fit to the contact portion of the voltage–distance curve. The cantilever deflection (d) is finally converted to force, F, using F = d*k (assuming calibrated cantilever spring constant, k). Force-displacement curves can be roughly divided in three regions, the contact line, the non-contact region, and the zero line (Fig. 6). The elasto-plastic behavior of materials can be determined from the contact lines of force-displacement once they are considered ideally elastic materials [12,24].

According to line ab in Fig. 6, the cantilever is undeflected and far from the surface. The slope of line dc can be considered Young's
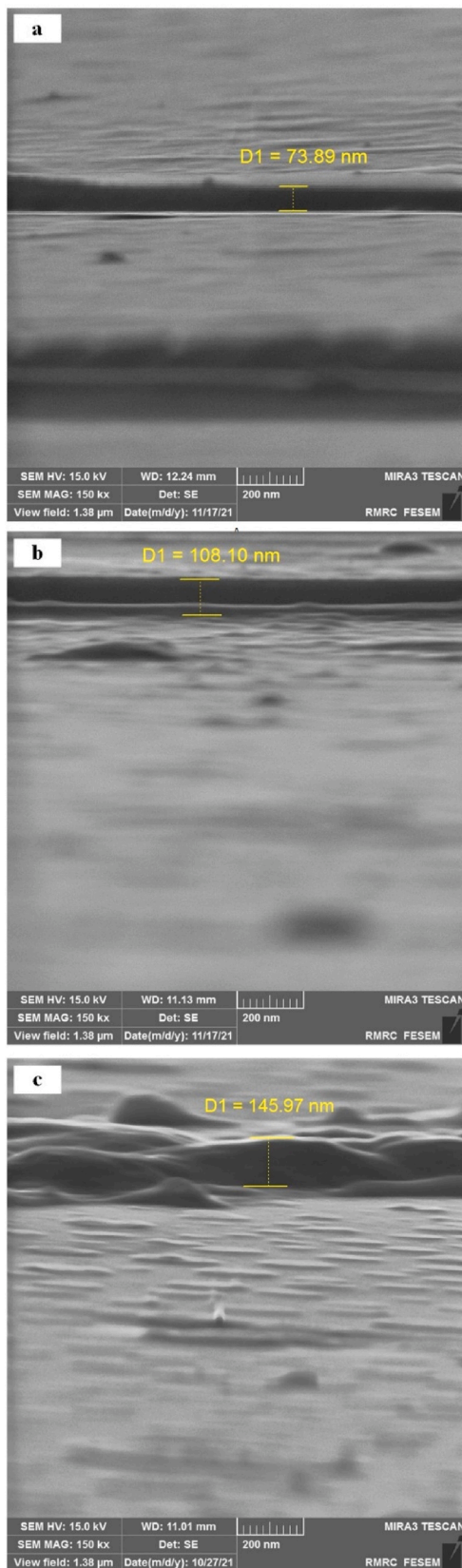
Fig. 3. SEM images of the cross section of morphology of samples; (a) Un coated, (b) Zn coated, (c) Mg-Zn coated, (d) Zn-Mg-Zn coated.

modulus of the material. While the cantilever is trying to jump off the contact, adhesion forces may occur and cause the cantilever to adhere to the surface (Fig. 6, points (c)–(b)). Adhesion force can be measured based on the difference between these two curves.

The elastic modulus of the samples was evaluated using the approach of Kracke and Damaschke [12]. The effective young's modulus was determined using the following equation: (2):

$$dF \Big/ d(\Delta z) = \left(2 \Big/ \sqrt{\pi}\right) Ee\sqrt{A} \tag{2}$$

In this equation.

Where, dF/d(Δz) is the slope of the contact region in the Force-Displacement curve, A denotes the contact area between the AFM tip and the sample, and Ee is the effective Young's modulus.

The elastic modulus of the sample (E) was then determined using the relationship between the effective modulus and the material properties of both the sample and the AFM tip:

$$\frac{1}{Ee} = \frac{\left(1 - \vartheta tip^2\right)}{Etip} + \frac{\left(1 - \vartheta^2\right)}{E} \tag{3}$$
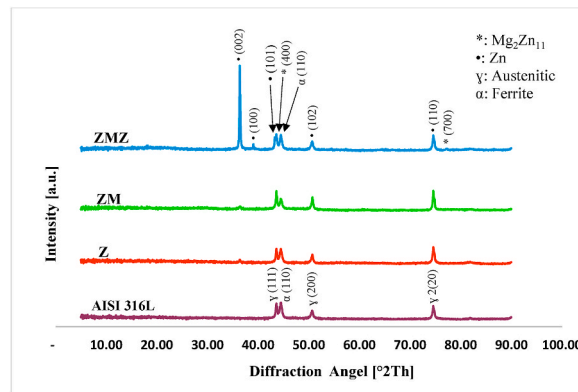

Fig. 4. X-ray diffraction analysis for uncoated and coated samples.

Table 1
Crystallite size, FWHM and interplanar spacing of uncoated and coated samples.

| Sample	2θ (°)	d-spacing (A°)	FWHM (Radian)	Crystallite size (nm)
SS	43.57	2.07	0.1560	12.26
	44.46	2.03	0.3744	5.18
	50.64	1.80	0.3744	5.83
	64.45	1.44	0.1872	17.16
	74.56	1.27	0.1872	27.81
	81.80	1.17	0.4992	19.46
Z	36.36	2.46	0.2047	8.40
	43.58	2.07	0.1535	12.46
	44.47	2.03	0.3582	5.42
	50.69	1.79	0.2558	8.55
	74.58	1.27	0.1535	33.95
ZM	36.44	2.46	0.2558	6.73
	43.59	2.07	0.1279	14.96
	44.49	2.03	0.3582	5.42
	50.71	1.79	0.2558	8.55
	74.58	1.27	0.1535	33.95
ZMZ	39.03	2.30	0.1535	11.62
	43.26	2.08	0.0936	20.33
	43.58	2.07	0.1872	10.22
	44.44	2.03	0.1872	10.36
	50.60	1.80	0.1872	11.66
	54.37	1.68	0.1248	19.06
	64.38	1.44	0.1872	17.12
	74.56	1.27	0.1560	33.37
	77.17	1.23	0.1872	33.34
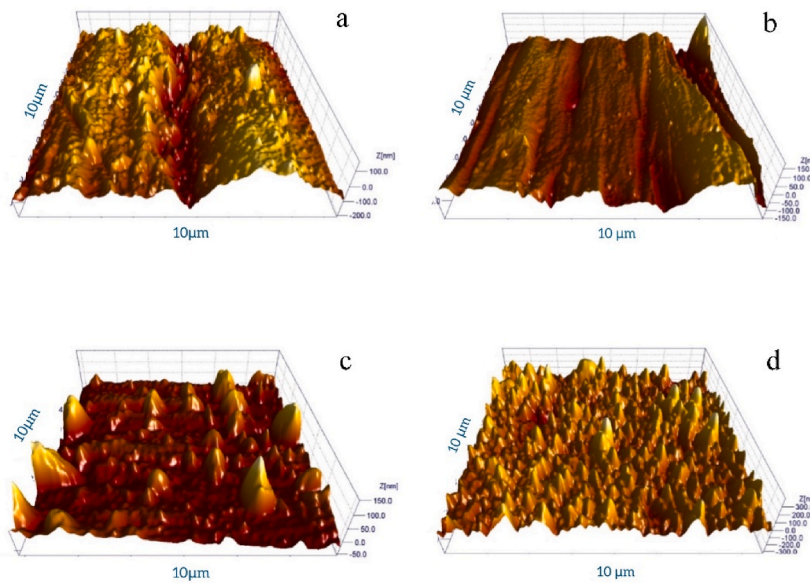
Fig. 5. AFM images of samples, (a) Un coated, (b) Zn coated; (c) Mg-Zn coated, (d) Zn-Mg-Zn coated.

Table 2
AFM roughness results of uncoated and coated samples.

Sample	R_a (nm)	S_a (nm)	S_q (nm)
SS	35.88	41.32	53.26
Z	21.83	30.23	39.89
ZM	25.50	32.90	40.18
ZMZ	28.48	33.05	42.99

Where:

E_{tip} and ϑ tip are the elastic modulus and Poisson's ratio of the AFM tip, respectively. E and ϑ are the elastic modulus and Poisson's ratio of the sample, respectively.

In this study, the simplest model was employed, which assumes a tip with a circular contact area. The contact radius was estimated to be 5 nm, corresponding to the curvature radius of the tip apex as provided by the manufacturer. The elastic modulus and Poisson's ratio of the AFM tip were assumed to be 130 GPa and 0.27, respectively [12,24].

The results of the AFM test can be found in Table 3. The average elastic modulus in the uncoated sample and one-layer, two-layer, and three-layer samples was 225.5, 24.72, 21.42, and 29.65 GPa, respectively. As can be seen, the elastic modulus significantly decreased in the coated samples. The elastic modulus of Zn monolayer (Z), Zn-Mg bilayer (ZM), and Zn-Mg-Zn triple-layer (ZMZ) coatings were much lower than uncoated stainless steel. All these values are within the range of elastic modulus of human cortical bone (10–30 GPa) (P). Moreover, the Zn-Mg bilayer showed the lowest elastic modulus. A lower elastic modulus in implants is crucial for
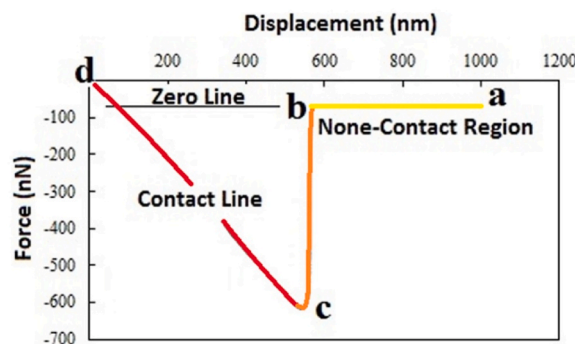

Fig. 6. Different parts of the force-displacement curve for surface of samples.

Table 3
Elastic modulus results of uncoated and coated samples measured via AFM.

Sample	Elastic modulus (GPa)	Standard deviation
SS	225.5	72.01
Z	24.72	4.61
ZM	21.42	5.68
ZMZ	29.65	7.44

minimizing the undesirable complication of stress shielding. Stress shielding refers to the phenomenon where the implant, due to its higher elastic modulus compared to bone, absorbs more of the mechanical load. This imbalance reduces the mechanical stress on the surrounding bone, leading to bone resorption and potential loosening of the implant-bone coupling over time.

3.3. Wettability

Upon contact with the culture or intercellular fluids or blood, the outer surface of the implant tends to uptake more protein, which leads to cell adhesion. Examination of cell adhesion to the surface shows that cell surface interactions are often influenced by free energy, chemistry, and topography of the substrate surface. Improvement of these properties via surface modification has become a general method for promoting cellular interaction.

Surface energy and physical properties of the surface can be determined by the contact angle of liquids with the surface. The Yang equation [5] describes the equilibrium of the contact angle of a drop on a smooth surface θ_0, is as follows:

$$\theta = \frac{(\gamma_{LV} - \gamma_{SL})}{\gamma_{LV}} \tag{5}$$

Where, γ_{SV}, γ_{SL}, and γ_{LV} are surface tensions per unit length of solid-vapor, liquid-solid, and liquid-vapor, respectively. θ also denotes the contact angle of the junction (LV) with (SV). Greater contact angles mean the higher hydrophobicity. In this case, the liquid cannot expand to a larger solid surface. Unlike the first case, the lower contact angle indicates that the solid is more hydrophilic and maximizes the adhesion of the liquid to its surface [5]. Surface roughness is an important factor in the contact angle, hydrophilicity, and hydrophobicity of the surface. The higher the surface roughness, the greater its hydrophilicity.
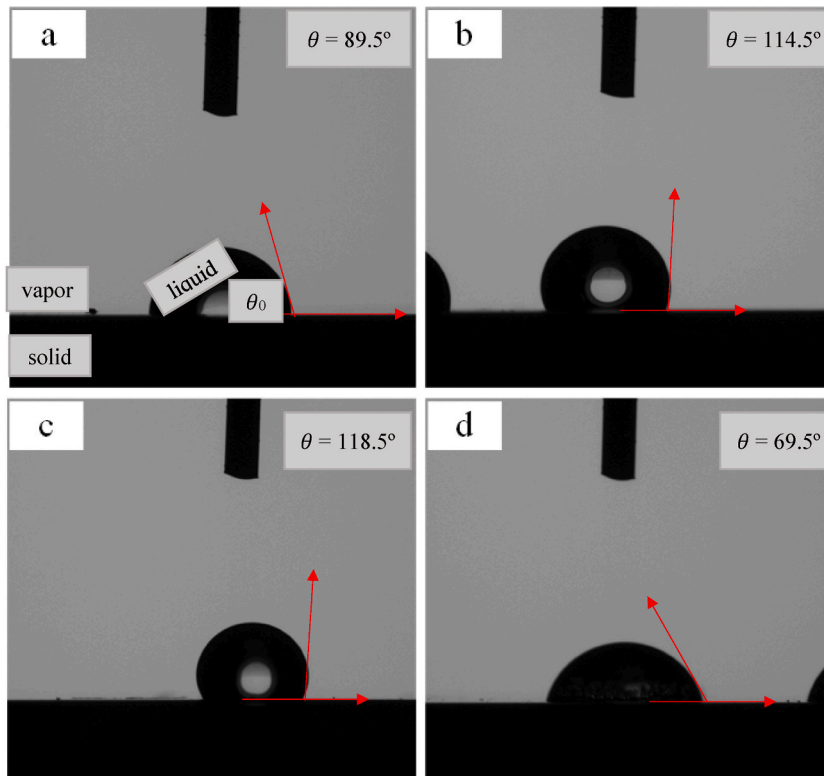

Fig. 7. Contact angle images for surface; (a) Un coated, (b) Zn coated, (c) Mg-Zn coated, (d) Zn-Mg-Zn coated.

Previous studies have also shown that surfaces with contact angles of 40–70° and moderate wettability are the most suitable surfaces for cell adhesion. The results of the contact angle test are shown in Fig. 7(a–d). As seen, the contact angles in uncoated samples, as well as those with one-layer, two-layer and three-layer coatings are equal to 89.5°, 114.5°, 118.5°, and 69.5°, respectively.

The scattering of most peaks and valleys in these samples caused a uniform nano-sized roughness. The average surface roughness of the samples with one and two layers is smaller than that of the three-layer sample. The results of this test show that the sample with ZMZ three-layer coating has the lowest contact angle and becomes hydrophilic after coating.

3.4. Antibacterial activity

Images of plates containing *E.coli* bacterial colonies are shown in Fig. 8(a–d). A comparison of coated and uncoated samples indicates substantially less adhesion and bacterial growth on coatings with Zn and Mg elements. As can be seen, the white spots are *E.coli* bacteria. The uncoated sample showed no bactericidal effect. In the one-layer sample, a small number of bacteria around the coating were killed, giving rise to a small inhibition zone of almost 3 mm. In the sample with two-layer coating, a larger inhibition zone (8 mm) can be seen which can be due to the simultaneous presence of Zn and Mg elements. Three-layer sample exhibited a larger inhibition zone (15 mm) as its Zn content was twice that of the one- and two-layer samples. It also included Mg.

As reported earlier, Zn and Mg coatings can significantly inhibit the growth of *E.coli* bacteria. The antibacterial mechanism of Mg involves the decomposition of this element at the implant site which increases the pH, affecting both *Staphylococcus aureus* and *E.coli* [25]. The results of antibacterial tests also indicated that Zn can increase the number of anti-adhesion bacteria. Zn^{2+} ions form strong bonds with the amino and carboxyl groups of the membrane, changing the surface chemistry of bacteria and inactivating them [21].

In general, all three coated samples showed antibacterial properties, but the inhibition zone of the three-layer sample was larger than the other samples such that the difference between the dose containment area of three-layer coating with the sample with one-layer and two-layer coating was 12 and 7 mm, respectively.

3.5. Release ions

It is highly important in medical science to determine the release of metal elements from samples due to their essential role in the biological reactions in the body. Some metal ions, such as Zn, Mg, Cu, and Fe, are naturally present in the body, and their presence is essential for the normal functioning of the body. However, the concentration of these metal ions in the body can be detrimental. It is critical to know the required amount of the elements in the body, as higher concentrations of these ions can cause poisoning.
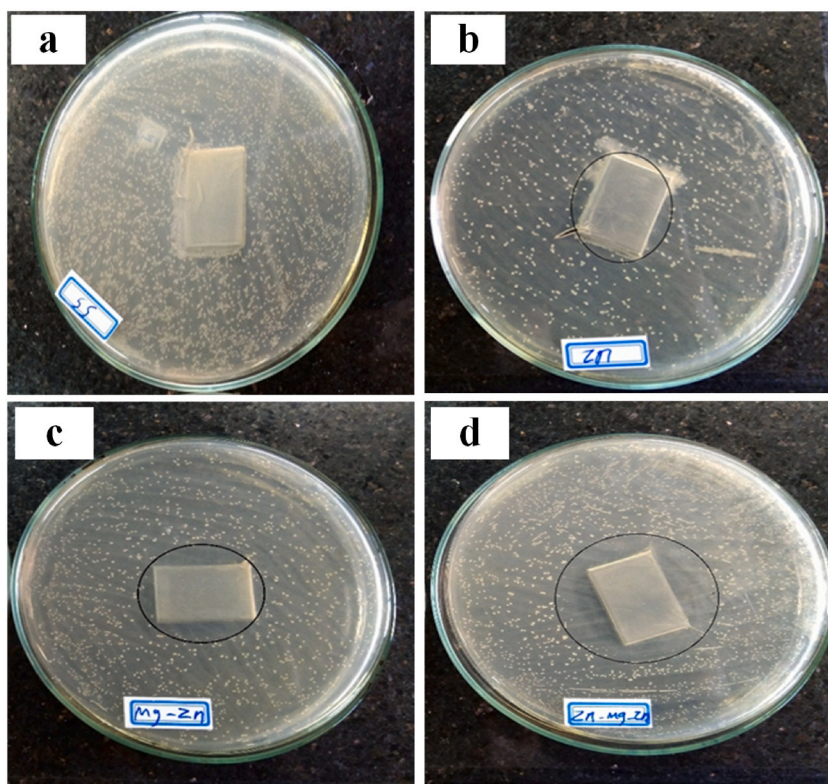

Fig. 8. Plates containing E. coli bacterial colonies for surface of samples; (a) Un coated, (b) Zn coated, (c) Mg-Zn coated, (d) Zn-Mg-Zn coated.

Table 4

The release of Ni^{2+}, Mg^{2+} and Zn^{2+} ions from coated and uncoated samples in SBF solution for 24 h at 37 °C.

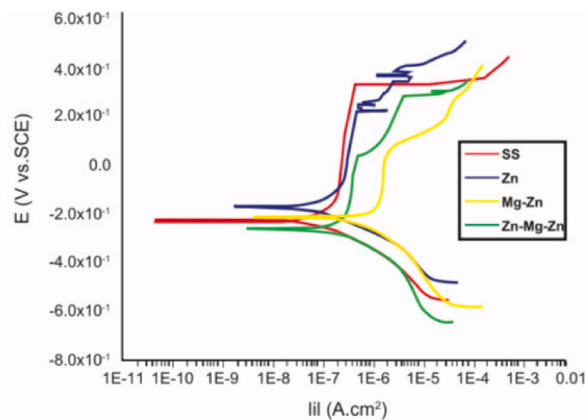| Sample	Ni^{2+} (PPM)	Mg^{2+} (PPM)	Zn^{2+} (PPM)
SS	0.056	0	0
Z	0.054	0	0.569
ZM	0.062	1.222	0.027
ZMZ	0.067	0.668	0.015

Fig. 9. Potentiodynamic polarization curves for uncoated and coated samples in in SBF solution for 30 min.

Previous studies [25,26] have suggested that low release of Zn^{2+} ions increase cell migration, proliferation, adhesion, and survival, while high release of Zn^{2+} ions can lead to cytotoxicity and DNA damage.

A previous study reported that the release of the allowable concentration of Mg^{2+} ions around degradable Mg alloys could increase the uptake, growth, cell proliferation, and adhesion of osteocytes at the implant surface, thereby, increasing the biocompatibility [25].

In this experiment, the release profiles of Zn^{2+}, Mg^{2+}, and Ni^{2+} ions were evaluated to ensure that their release remains within permissible limits. The release tests were conducted using a simulated body fluid (SBF) solution. According to Table 4, the zinc ions releasing has been decreased in the three-layer coating compared to the two-layer and single-layer coating. The magnesium ions releasing has also been decreased in the three-layer coating in comparison to the two-layer coating. These results show that the more the number of the layers, the better the adhesion of the coating. The results showed that these coatings do not cause problems for patients.

The presence of zinc layer on the surface of the substrate improved the coating adhesion to the substrate while declining the release of Mg^{2+} and Zn^{2+}. The release of Ni^{2+} was almost the same as in uncoated sample.

3.6. Electrochemical properties

The corrosion test results presented in Fig. 9 and Table 5 reveal important insights into the performance of the coatings applied to the stainless-steel substrates. Key parameters such as corrosion potential (E_cor), corrosion current (I_cor), polarization resistance (R_p), and coating resistance ($R\_coating$) were used to evaluate the effectiveness of the coatings in preventing corrosion. The dissolution of the Zn-Mg alloys coating involves the anodic reaction and the cathodic reaction are related to the substrate. During corrosion process, the anode is sacrificed and so the substrate does not corrode until the coating is completely removed, thereby the anode protects the substrate.

The corrosions equation of Zn-Mg alloy are as follows:

$$Zn \longrightarrow Zn^{2+} + 2e^- \tag{6}$$

Table 5

Polarization parameters of uncoated and coated samples.

Sample	R_coating (mpy)	E_cor (mpy)	I_cor (mpy)	R_p (mpy)
SS	2.77×10^8	−220	4.9×10^{-8}	40.82×10^7
Z	374250	−180	10^{-7}	31.23×10^7
ZM	32155	−190	6.5×10^{-7}	61.53×10^6
ZMZ	1.33×10^6	−270	1.5×10^{-7}	13.33×10^7

$$Mg \longrightarrow Mg^{2+} + 2e^- \tag{7}$$

The corrosion resistance of the uncoated and Z, ZM, and ZMZ coated specimens were 40.82×107, 31.23×107, 61.53×106, and 13.33×107 (mpy) respectively. Observations showed that the uncoated stainless steel exhibited the highest corrosion resistance among all samples, attributed to the naturally occurring chromium carbide layer on its surface, which provides excellent corrosion resistance. In the one-layer coating the corrosion resistance of the Zn-coated sample was lower than that of the uncoated sample but still provided a level of protection. The Zn coating likely acts as a sacrificial anode, reducing the corrosion rate of the substrate but not to the extent of the uncoated sample.

Two-layer sample coating exhibited a further reduced corrosion resistance compared to the Zn-coated sample. The inclusion of magnesium in the coating may have affected the overall protective performance, possibly due to its own corrosion characteristics or interaction with the substrate and the triple-layer coating showed an improved corrosion resistance compared to the Zn-Mg coating but was still lower than the uncoated stainless steel. The additional Zn layer in this coating could be providing some sacrificial protection, though it may not fully compensate for the corrosion resistance lost due to the introduction of magnesium.

The surface structure has been previously mentioned in the scientific literature [26,27]. The results indicate that while the coatings provide varying levels of protection, they do not surpass the natural corrosion resistance provided by the chromium carbide layer of the uncoated stainless steel. The lower corrosion resistance in coated samples can be attributed to the nature of the coating materials and their interaction with the corrosive environment. The coatings, especially those with magnesium, may undergo corrosion themselves, which could affect the overall protection of the substrate.

In conclusion, the uncoated stainless steel remains superior in terms of corrosion resistance. However, the coatings may offer other benefits such as improved biocompatibility or mechanical properties, which should be considered based on the intended application.

4. Conclusions

In this study, zinc and multi-layer zinc-magnesium coatings were applied to AISI 316L stainless steel substrates using thermal evaporation to enhance antibacterial properties and reduce the elastic modulus. The growth of zinc and magnesium particles on the surface of the substrate was confirmed by FE-SEM images, while EDX analysis indicated the presence and uniform distribution of zinc and magnesium elements on the surface of the substrate. AFM findings showed that coated samples had a more uniform surface roughness compared to uncoated samples, indicating a smoother surface quality Coated samples exhibited a significant reduction in elastic modulus, bringing the values closer to those of human cortical bone. This reduction enhances the biocompatibility of the coatings by mitigating stress shielding effects, which can lead to bone atrophy around implants. The three-layer coating displayed a lower contact angle, indicating increased hydrophilicity compared to the uncoated sample. This suggests that the coated samples may have improved interaction with biological fluids. The results of antibacterial test also showed the antibacterial activity of the coated samples against Gram-negative *Escherichia coli* compared to the uncoated sample due to the formation of a larger inhibition area. The three-layer sample showed the highest antibacterial properties and the largest inhibitory zone. Examination of the atomic spectrometer showed that in the sample with three layers of zinc and magnesium, the rate of ion emission is reduced compared to the sample with two layers. The two-layer sample, however, exhibited lower zinc ions release compared to the one-layer sample. Overall, the study highlights that the multi-layer coatings not only improve mechanical and biological properties but also provide better control over ion release and corrosion resistance compared to single-layer coatings.

CRediT authorship contribution statement

Bahare Soltani: Writing – original draft, Validation, Investigation. **Sayed Mahmood Rabiee:** Writing – review & editing, Supervision, Project administration, Funding acquisition, Data curation, Conceptualization. **Salman Nourouzi:** Validation, Supervision, Funding acquisition, Conceptualization. **Seyed Jamal Hosseinipour:** Validation, Supervision, Project administration, Formal analysis, Data curation, Conceptualization. **Simindokht Khademjafari:** Writing – review & editing, Validation, Methodology, Formal analysis.

Declaration of competing interest

The authors declare that they have no known competing financial interests or personal relationships that could have appeared to influence the work reported in this paper.

Acknowledgments

References

[1] T. Yetim, H. Tekdir, M. Taftalı, K. Turalıoğlu, A.F. Yetim, Synthesis and characterisation of single and duplex ZnO/TiO2 ceramic films on additively manufactured bimetallic material of 316L stainless steel and Ti6Al4V, Surf. Topogr. Metrol. Prop. (2023 Feb 11) 024005.
[2] J.A. Disegi, L. Eschbach, Stainless steel in bone surgery, Injury 31 (2000 Dec 1) D2–D6.

[3] K.V. Sudhakar, Metallurgical investigation of a failure in 316L stainless steel orthopaedic implant, Eng. Fail. Anal. 12 (2) (2005 Apr 1) 249–256.

[4] D. Sivaraj, K. Vijayalakshmi, Enhanced antibacterial and corrosion resistance properties of Ag substituted hydroxyapatite/functionalized multiwall carbon nanotube nanocomposite coating on 316L stainless steel for biomedical application, Ultrason. Sonochem. 59 (2019 Dec 1) 104730.

[5] R. Alias, R. Mahmoodian, M.H. Abd Shukor, Development and characterization of a multilayer silver/silver-tantalum oxide thin film coating on stainless steel for biomedical applications, Int. J. Adhesion Adhes. 92 (2019 Jul 1) 89–98.

[6] C. Zhao, H. Wu, P. Hou, J. Ni, P. Han, X. Zhang, Enhanced corrosion resistance and antibacterial property of Zn doped DCPD coating on biodegradable Mg, Mater. Lett. 180 (2016 Oct 1) 42–46.

[7] C. Yao, W. Chen, W. Gao, Codeposited Zn–Mg coating with improved mechanical and anticorrosion properties, Surf. Coating. Technol. 219 (2013 Mar 25) 126–130.

[8] S. Chowdhury, M.T. Laugier, The use of non-contact AFM with nanoindentation techniques for measuring mechanical properties of carbon nitride thin films, Appl. Surf. Sci. 233 (1–4) (2004 Jun 30) 219–226.

[9] H. Tekdir, T. Yetim, A.F. Yetim, Corrosion properties of ceramic-based TiO2 films on plasma oxidized Ti6Al4V/316L layered implant structured manufactured by selective laser melting, Journal of Bionic Engineering 18 (2021 Aug) 944–957.

[10] S. Khademjafari, S.M. Rabiee, S. Nourouzi, R.S. Rami, In-vitro evaluation and antibacterial activity of ZnO nanoparticles deposited on hydroxyapatite tablets by RF magnetron sputtering, Mater. Today Commun. 28 (2021 Sep 1) 102520.

[11] M. Zhu, Y. Lu, C. Zhang, L. Li, M. Xie, J. Lin, K. Tang, Facile fabrication of Mg-based coating to improve the biodegradable behavior and cytocompatibility of pure zinc, Surf. Coating. Technol. 372 (2019 Aug 25) 209–217.

[12] H.R. Bakhsheshi-Rad, E. Hamzah, H.T. Low, M. Kasiri-Asgarani, S. Farahany, E. Akbari, M.H. Cho, Fabrication of biodegradable Zn-Al-Mg alloy: mechanical properties, corrosion behavior, cytotoxicity and antibacterial activities, Mater. Sci. Eng. C 73 (2017 Apr 1) 215–219.

[13] X. Wang, X. Wang, D. Wang, M. Zhao, F. Han, A novel approach to fabricate Zn coating on Mg foam through a modified thermal evaporation technique, J. Mater. Sci. Technol. 34 (9) (2018 Sep 1) 1558–1563.

[14] Y. Su, K. Wang, J. Gao, Y. Yang, Y.X. Qin, Y. Zheng, D. Zhu, Enhanced cytocompatibility and antibacterial property of zinc phosphate coating on biodegradable zinc materials, Acta Biomater. 98 (2019 Oct 15) 174–185.

[15] E. Zhang, X. Zhao, J. Hu, R. Wang, S. Fu, G. Qin, Antibacterial metals and alloys for potential biomedical implants, Bioact. Mater. 6 (8) (2021 Aug 1) 2569–2612.

[16] S. Sabooni, E. Galinmoghaddam, A.A. Turkin, L.Q. Lu, R.J. Westerwaal, C. Boelsma, E. Zoestbergen, Y.T. Pei, Tailoring vapor-deposited ZnMg–Zn bilayer coating for steels by diffusion-driven phase transformation, J. Alloys Compd. 836 (2020 Sep 25) 155448.

[17] T. Yetim, Corrosion behavior of Ag-doped TiO$_2$ coatings on commercially pure titanium in simulated body fluid solution, Journal of Bionic Engineering 13 (3) (2016 Jul 1) 397–405.

[18] B. Bhushan, T. Kasai, A surface topography-independent friction measurement technique using torsional resonance mode in an AFM, Nanotechnology 15 (8) (2004 Jun 9) 923.

[19] B. Kracke, B. Damaschke, Measurement of nanohardness and nanoelasticity of thin gold films with scanning force microscope, Appl. Phys. Lett. 77 (3) (2000 Jul 17) 361–363.

[20] S. Sabooni, E. Galinmoghaddam, M. Ahmadi, R.J. Westerwaal, J. Van de Langkruis, E. Zoestbergen, J.T. De Hosson, Y.T. Pei, Microstructure and adhesion strength quantification of PVD bi-layered ZnMg-Zn coatings on DP800 steel, Surf. Coating. Technol. 359 (2019 Feb 15) 227–238.

[21] R. Jain, R. Pitchumani, Fabrication and characterization of zinc-based superhydrophobic coatings, Surf. Coating. Technol. 337 (2018 Mar 15) 223–231.

[22] Y.H. Zou, J. Wang, L.Y. Cui, R.C. Zeng, Q.Z. Wang, Q.X. Han, J. Qiu, X.B. Chen, D.C. Chen, S.K. Guan, Y.F. Zheng, Corrosion resistance and antibacterial activity of zinc-loaded montmorillonite coatings on biodegradable magnesium alloy AZ31, Acta Biomater. 98 (2019 Oct 15) 196–214.

[23] J. Kubásek, D. Dvorský, J. Šedý, Š. Msallamová, J. Levorová, R. Foltán, D. Vojtěch, The fundamental comparison of Zn–2Mg and Mg–4Y–3Re alloys as a perspective biodegradable materials, Materials 12 (22) (2019 Nov 13) 3745.

[24] J. Ma, N. Zhao, D. Zhu, Endothelial cellular responses to biodegradable metal zinc, ACS Biomater. Sci. Eng. 1 (11) (2015 Nov 9) 1174–1182.

[25] Z. Lin, X. Sun, H. Yang, The role of antibacterial metallic elements in simultaneously improving the corrosion resistance and antibacterial activity of magnesium alloys, Mater. Des. 198 (2021 Jan 15) 109350.

[26] J.M. Byun, S.R. Bang, H.W. Kim, T.Y. Kim, S.J. Hong, Y. Do Kim, Effect of heat treatment on corrosion resistance and adhesion property in Zn-Mg-Zn multi-layer coated steel prepared by PVD process, Surf. Coating. Technol. 309 (2017 Jan 15) 1010–1014.

[27] O. Çomaklı, M. Yazıcı, A. Atmaca, T. Yetim, The electrochemical and tribocorrosion behavior of hybrid ceramic film-coated Ti alloys, Ceram. Int. 50 (5) (2024 Mar 1) 7988–7997.